Published in final edited form as:
Phys Med Biol. 2011 May 21; 56(10): 3091–3106. doi:10.1088/0031-9155/56/10/013.

Design and performance evaluation of a whole-body Ingenuity TF PET–MRI system

H Zaidi[1,2,5], **N Ojha**[3], **M Morich**[3], **J Griesmer**[3], **Z Hu**[3], **P Maniawski**[3], **O Ratib**[1], **D Izquierdo-Garcia**[4], **Z A Fayad**[4], and **L Shao**[3]

[1]Division of Nuclear Medicine and Molecular Imaging, Geneva University Hospital, CH-1211 Geneva, Switzerland [2]Geneva Neuroscience Center, Geneva University, CH-1205 Geneva, Switzerland [3]Philips Healthcare, Cleveland, OH, USA [4]Translational and Molecular Imaging Institute, Mount Sinai School of Medicine, New York, USA

Abstract

The Ingenuity TF PET–MRI is a newly released whole-body hybrid PET–MR imaging system with a Philips time-of-flight GEMINI TF PET and Achieva 3T X-series MRI system. Compared to PET–CT, modifications to the positron emission tomography (PET) gantry were made to avoid mutual system interference and deliver uncompromising performance which is equivalent to the standalone systems. The PET gantry was redesigned to introduce magnetic shielding for the photomultiplier tubes (PMTs). Stringent electromagnetic noise requirements of the MR system necessitated the removal of PET gantry electronics to be housed in the PET–MR equipment room. We report the standard NEMA measurements for the PET scanner. PET imaging and performance measurements were done at Geneva University Hospital as described in the NEMA Standards NU2-2007 manual. The scatter fraction (SF) and noise equivalent count rate (NECR) measurements with the NEMA cylinder (20 cm diameter) were repeated for two larger cylinders (27 cm and 35 cm diameter), which better represent average and heavy patients. A NEMA/IEC torso phantom was used for overall assessment of image quality. The transverse and axial resolution near the center was 4.7 mm. Timing and energy resolution of the PET–MR system were measured to be 525 ps and 12%, respectively. The results were comparable to PET–CT systems demonstrating that the effect of design modifications required on the PET system to remove the harmful effect of the magnetic field on the PMTs was negligible. The absolute sensitivity of this scanner was 7.0 cps kBq^{-1}, whereas SF was 26%. NECR measurements performed with cylinders having three different diameters, and image quality measurements performed with IEC phantom yielded excellent results. The Ingenuity TF PET–MRI represents the first commercial whole-body hybrid PET–MRI system. The performance of the PET subsystem was comparable to the GEMINI TF PET–CT system using phantom and patient studies. It is conceived that advantages of hybrid PET–MRI will become more evident in the near future.

[5]Author to whom any correspondence should be addressed.

1. Introduction

Positron emission tomography (PET) imaging is widely used clinically for its unique ability for molecular imaging, especially in oncology, cardiology and neurology. Nowadays, PET is combined with computed tomography (CT) imaging in hybrid PET–CT scanners where CT provides the anatomical underlay for localization of abnormalities visualized on PET images. However, CT imaging with its poor soft-tissue contrast is less than ideal for several applications most notably in brain, head/neck and prostate imaging (Zaidi and Mawlawi 2007).

The idea of combining a PET to a magnetic resonance imaging (MRI) system, for the latter's superior soft-tissue contrast, was proposed even before PET–CT was commercially developed. More than 10 years ago Marsden and Cherry developed the first simultaneous PET–MRI system (Shao *et al* 1997). The single-slice preclinical PET system was placed inside the receiver coil of the MRI, and was coupled to photomultiplier tubes (PMTs) housed outside the main magnetic field via long optical fibers. The drawback of this prototype was that the PET signal quality was degraded from optical loss caused by light transmission via optical fibers. Pichler *et al* have since designed a full PET detector ring which can be operated in the MR scanner without the need of optical fiber coupling (Judenhofer *et al* 2008). This PET scanner prototype, based on avalanche photodiodes, was initially designed for preclinical imaging and has now been applied for brain imaging inside a 3T clinical whole-body MRI system (Schlemmer *et al* 2008). Until such technology becomes available for whole-body imaging, other approaches for so-called sequential PET–MR imaging have been researched (Delso and Ziegler 2009).

The Philips Ingenuity TF PET–MRI is a hybrid imaging system with Philips time-of-flight GEMINI TF PET and Achieva 3T X-series MRI system, as shown in figure 1 (Gagnon *et al* 2008). While this design does not allow simultaneous PET and MRI acquisition, it allows acquisition of automatically co-registered PET and MR images acquired sequentially, similar to the workflow in PET–CT systems. Key parameters of the Achieva 3T MRI system are described in table 1. Following initial development, two PET–MRI systems were installed in Mount Sinai Medical Center, NY and Geneva University Hospital, Geneva. In this study, we evaluate the imaging characteristics of the PET component of the Ingenuity TF PET–MRI scanner using the National Electrical Manufacturers Association (NEMA) NU2-2007 Standards measurements (NEMA 2007). Additional measurements were done to evaluate the mutual interference between the two systems on imaging performance and the impact on reconstructed images.

2. Materials and methods

2.1. PET–MR scanner design and intrinsic measurements PET detector and electronics

The PET detector and acquisition system electronic hardware for the PET–MR system was based on the existing GEMINI TF PET–CT electronic hardware, with requisite changes to allow for compatibility in the MR scanner environment (Surti *et al* 2007). Key specifications of the PET scanner are listed in table 2. Signal readout on the PET is performed by a hexagonal array of 420 PMTs of 38 mm diameter. The Anger-logic detector has

characteristics of good crystal separation with uniform light collection and energy resolution (Karp *et al* 2003, Surti *et al* 2000). The hardware coincidence-timing window for this scanner is set at 6 ns, and a delayed coincidence window technique is used to estimate the random coincidences in collected data.

The PMT operating voltage is nominally set between 1100 and 1500 V dc for imaging to detect the photons generated from the crystal detector array during the photon interaction with the detector. The LYSO detector blocks themselves are slightly radioactive and emit beta rays that interact within the crystal block and cause photons to be emitted. These background photons randomly cause normal light signals in the PMTs sending an electrical signal to the connected electronics channel. The resulting wide spectrum electromagnetic pulse caused an increase in the MR background noise floor. To minimize this effect, we designed the system to reduce the PMT high voltage to 900 V dc while acquiring MR data. The voltage is reset to the nominal value after the MR is finished, before PET acquisition is started. Our measurements indicate that essentially no time delay was necessary for stabilizing the PMTs if the high voltage was reduced. Figure 2 shows that measured count density, energy and timing resolution are well-within system specifications after a series of reduction cycles in PMT voltage.

Mitigation of magnetic field effects—The PET scanner was redesigned to operate inside a standard MR scan room. The key design goal was to place both MR and PET as close as possible without loss of image quality. The PET was placed coaxial at a distance of 4.2 m from the MR (distance between centers of FOV) which provided good compromise between magnetic flux at PET, PET–MR system footprint and acceptable patient imaging workflow. Even fringe 3T active-shield magnetic fields at such a distance were measured to be close to 20 times the Earth's magnetic field, which rendered PET PMTs non-functional, necessitating the need for magnetic shielding for their operation. PMTs are very sensitive to magnetic flu the presence of which deflects the PMT photoelectrons from their trajectories resulting in reduced pulse height (an apparent gain change) (Delso and Ziegler 2009).

Simulations of the magnetic flux indicated that the required low flux at the PMTs could be achieved by introducing bulk, but relatively thin, magnetic shielding in the PET gantry without the need for any material in the normal PET imaging path for the annihilation photons. Magnetic flux simulations were done using Vector Fields software, Aurora, IL, USA. The PET gantry was thus redesigned with a modest permeability laminated steel shield around the detector light box to guide most of the fringe magnetic field around the PMTs (DeMeester *et al* 2009). Inside the light box, higher permeability local PMT shields were used to further reduce the residual magnetic field over individual PMTs. Figure 3 shows a simulation of the magnetic field at the PMTs in the PET gantry with magnetic shielding in place for the PET gantry portion. The PMT gains of the PET system were recalibrated 'at field' to remove the effect of the remaining residual magnetic field at the PMTs. The additional magnetic material in the room was sufficiently far away from the magnet center to allow the use of normal procedures in the shimming of the 3T magnet.

MRI magnet main magnetic field B_0 homogeneity in the FOV was measured after standard MRI shimming procedure before and after the PET gantry was installed in the PET–MR

suite. B0 homogeneity was calculated on the characterization volumes based on spherical harmonic representation of the data, as determined from 24-plane, 24-angle measurements on a larger volume (table 3).

Mitigation of RF noise—3T MRI corresponds to a proton imaging frequency of ~128 MHz, but is sensitive to frequencies in the range of 32–128 MHz (e.g. for multinuclear). RF noise generated from electronics situated inside the PET gantry shows distinct MR artifacts (Slates *et al* 1999, Wehrl *et al* 2009). While a normal PET system has EMI emissions that meet all regulatory requirements, requirements for MRI are far more stringent. To obviate these issues, PET system modifications were done to move all electronics from the PET gantry to the equipment room where it is easier to mitigate spurious noise transmissions. The PET gantry contained only the normal crystal/PMT geometry and the first level of signal processing boards. All power and signal cables penetrating the MR walls were filtered through specially designed RF penetration panels to prevent extraneous EMI radiation to enter the imaging suite through the cables into the room. Further, PET acquisition electronics were enclosed in an RF tight cabinet which provided shielding effectiveness of 40 dB at 1 GHz frequencies.

Energy and timing resolution—Energy correction tables were generated by using a ^{22}Na point source and calculating the peak position in the energy spectrum for each crystal and normalizing it to a common value (Surti *et al* 2007). To test the PET magnetic shielding, energy centroids and full width at half maximum (FWHM) per crystal were calculated with the MRI magnet ‘on’ (at field) and ‘off’ (ramped down), as shown in figure 4. A very minor energy resolution degradation of 0.1% FWHM (table 4) was observed with ramping up of the magnet demonstrating the effectiveness of magnetic shielding in removing the deleterious effect of the magnetic field from normal PMT operation.

Timing calibration was performed on the system as described before (Surti *et al* 2007) with the MRI magnet ramped down. After ramping up the MRI magnet, residual magnetic field at the PMTs altered timing resolution centroids as shown in figure 4. Recalibration of the PET system at field restored the overall timing resolution to the original value with a very minor increase of 7 ps.

2.2. PET scanner performance measurements

All PET calibrations and measurements were done with the MRI system ramped to 3T, shimmed and calibrated. Performance measurements were done at Geneva University Hospital on the Ingenuity TF PET–MRI scanner following the procedure outlined in the NEMA NU2-2007 standard (NEMA 2007).

Spatial resolution—Spatial resolution measurements were performed with point sources made by placing ^{18}F-FDG (fluorodeoxy glucose) in 1 mm capillary tubes. Measurements were performed at positions of (X,Y) equals (0,1), (0,10) and (10,0) cm in the transaxial plane. Axially, the point sources were placed at the center of the FOV and at one quarter of the extent of the axial FOV from the center (45 mm). Sinograms were reconstructed using the 3D Fourier reprojection (3D-FRP) algorithm (Matej and Lewitt 2001), with an

unapodized filter (ramp filter with a cutoff at the Nyquist frequency). Standard NEMA analysis was then performed to calculate the FWHM and the full width at tenth maximum (FWTM) of the point spread functions in radial, tangential and axial directions.

Sensitivity—The NEMA PET sensitivity phantom comprises five concentric aluminum sleeves with a wall thickness of 2.5 mm and length of 700 mm. A plastic line source with 2 mm diameter was filled with 8.8 MBq of ^{18}F (count losses and randoms were assumed to be negligible at this low activity) and threaded through the innermost sleeve. Count rates for 1 through 5 of the sleeves in-place were obtained from list-mode files and extrapolated to obtain the rate with zero thickness of aluminum under the assumption that all positrons would be annihilated in the absence of an attenuating material.

Scatter fraction and count rate measurements—The scatter fraction (SF) and count rate measurements were performed using the NEMA scatter phantom. The scatter phantom is a solid polyethylene cylinder (70 cm length, 20 cm diameter) with a water equivalent density of 1 g mL^{-1}. The phantom was threaded with a plastic tube (80 cm length, 3.2 mm diameter) filled with 555 MBq of ^{18}F placed at 4.5 cm radial offset from the center. Data were acquired at several time points as activity in the cylinder decayed over several half-lives until true event losses were less than 1% and processed as described before (Surti *et al* 2007). The prompt and delayed coincidence window data were acquired and rebinned using single-slice rebinning. Random events were measured from the delayed sinogram profile, whereas the prompt sinogram profile was used to calculate the number of scatter and random events within a region of interest (ROI) having a diameter of 24 cm (4 cm larger than the phantom's diameter). The final acquisition of the sequence with count loss rates and random rates below 1% of the true rates was used to determine the SF. For the last acquisition, it was assumed that random counts were negligible and only true and scatter counts constituted the total counts.

The SF was defined as

$$SF=\frac{\sum_i S_i}{\sum_i (S_i+T_i)}.$$

From the above calculations, noise equivalent count rate (NECR) was calculated using the relation

$$\mathrm{NECR}=\frac{\mathrm{Trues\ \ Rate}^2}{\mathrm{Trues\ \ Rate+Scatter\ \ Rate+Randoms\ \ Rate}}.$$

To better assess the performance of the scanner for heavy patients, the above count loss experiment was also acquired using two annular polyethylene sleeves of diameters 27 and 35 cm which were representative of an average and a large patient, respectively (Surti *et al* 2003). The calculation of scatter was performed within regions of 31 and 39 cm (diameter of cylinder + 4 cm) which was analogous to the NEMA method for the 20 cm diameter phantom.

Image quality—Image quality (IQ) measurements were performed using the NEMA/IEC torso phantom. The phantom was placed on the tabletop so that the sphere centers lay in the same axial plane close to the central slice in the scanner. The two largest spheres of the phantom were filled with water, whereas the other spheres were filled with activity equal to four times (and eight times in another scan) the background. To simulate activity from outside the FOV, the 20 × 70 cm NEMA phantom was abutted to the IEC phantom but outside the scan FOV.

MR-based attenuation correction (MRAC) of PET data was implemented for the IEC phantom. The intent of the NEMA IQ method is to test PET reconstructed image quality while applying the default clinical imaging workflow, acquisition protocol and reconstruction technique. The NEMA NU2-2007 standard was written for standalone PET and hybrid PET–CT systems, where it is assumed that a method for ac is readily available on the system, and that the same method is used for both clinical and phantom imaging. This methodology is not strictly applicable to PET–MRI as MRI does not provide a direct measurement of the amount of photon attenuation. Consequently, it was not possible with default MR acquisition techniques to directly translate the MR image into a PET attenuation map, as is done with CT images. It is perceived that custom MR acquisition and image processing methods may be needed for each phantom to be imaged with PET–MRI, if the MR is required to directly provide images that can be further processed on-the-fly to infer attenuation correction. Other solutions using pre-defined attenuation maps which are automatically applied during image reconstruction have also been proposed and are currently under evaluation (Zhang *et al* 2009, Morich *et al* 2010). We employed an MRAC technique which used image segmentation for the phantom, and template-based AC for the patient table.

The MR sequence (called *atMR* for attenuation correction MR sequence) used for IEC phantom imaging was slightly modified from the patient imaging sequence. A small flip angle of 2° was used to suppress the excess signal from water, and reduce dielectric artifacts from the MR images. A 2-segment MRAC image segmentation technique, with air and water being the two individual segments, was applied to the *atMR* images for the generation of the attenuation map of the IEC phantom. This method was essentially similar to the clinical MRAC technique (Hu *et al* 2009) but was modified to enable segmentation of the lung insert. Background air and water were segmented as separate volumes within the image and were assigned individual attenuation values. To estimate the attenuation from the plastic housing of the phantom, the phantom ac map was extended by one pixel (2 mm) in all dimensions. The attenuation from the patient table, which was also not visible in MR images, was estimated by appending a pre-defined attenuation template of the table to the segmented ac map of the phantom. PET images were reconstructed using a list-mode ordered-subsets expectation maximization (OSEM) technique using 3 iterations with 33 subsets each, a blob basis function, time-of-flight information and accounting for attenuation, scatter and random events in the system matrix.

Image analysis as defined by NEMA was performed on the acquired PET images to calculate background variability (BV) and contrast recovery coefficients (CRC) for each sphere. It should be understood that the above IQ method does not provide a framework for

testing the clinical MRAC technique, but is a robust test for overall PET IQ assuming an accurate phantom attenuation map is available.

Clinical studies—Clinical MRAC is a major challenge facing PET–MR imaging. Several techniques have been suggested for MRAC (Hofmann *et al* 2009), but few have been successfully implemented for whole-body imaging. We implemented a 3-segment (background air, soft tissue and lung) fully automated MRAC technique suitable for clinical whole-body imaging as described before (Hu *et al* 2009). The algorithm offers robust extraction of the outer contour of the body and the lungs. The *atMR* acquisition protocol consisted of a fast multi-stack whole-body protocol which took about 3 min for a 100 cm axial coverage. A 3D multi-stack spoiled T1 weighted gradient echo sequence was used with flip angle 10°, TE 2.3 ms, TR 4.1 ms, smallest water–fat shift, 600 mm transverse FOV with a slab thickness of 120 mm, voxel size $3 \times 3 \times 6$ mm^3, and 12 mm overlap between adjacent stacks. The *atMR* acquisition on its own is not intended to be a diagnostic quality image for MR purposes. The homogeneity of the main magnetic field B_0 may, for example, ultimately limit the FOV and require certain maximum stack thickness for the *atMR* acquisition.

Patients were scanned on the PET–MR scanner following a standard diagnostic PET–CT scan without additional tracer injection. The PET–MRI study consisted of survey images, a whole-body *atMR* sequence followed by the diagnostic PET scan. Further diagnostic MR scans were performed, if needed. Pre-generated attenuation maps of RF coils and accessories were automatically applied during PET reconstruction when present inside the PET FOV.

3. Results

3.1. PET scanner performance measurements

Spatial resolution—Table 5 summarizes the PET spatial resolution measurement results for the Ingenuity TF PET–MRI scanner compared to the GEMINI TF PET–CT scanner (Surti *et al* 2007). Spatial resolution was comparable in both systems demonstrating the effectiveness of magnetic shielding and overall system design which resulted in proper PMT calibration and operation.

Sensitivity—The absolute sensitivity of the Ingenuity TF PET–MRI scanner was 7000 cps MBq^{-1} when the line source was placed at the center of the scanner, and 7200 cps MBq^{-1} with a 10 cm radial offset. The axial sensitivity profile was triangular in shape (figure 5(A)) and peaked at about 160 cps MBq^{-1}.

Scatter fraction—Figure 5(B) shows the measured SF as a function of energy lower level discriminator (ELLD) for the 20 × 70 cm line source phantom. These results indicated that, as expected, raising the ELLD decreased system SF. The SF increased for all ELLD values as the phantom size increased due to increased photon attenuation and scatter. At the default ELLD value of 460 keV, the system SF was measured to be 26%, 35% and 42% for the 20 cm, 27 cm and 35 cm diameter cylinders, respectively. It should be noted that the ELLD in this investigation was set to 460 keV which is slightly higher than the standard setting on the GEMINI TF PET/CT scanner (440 keV) (Surti *et al* 2007).

Count rate performance—Figure 6 summarizes the results from count rate measurements for the three cylindrical phantoms. The total, true, random, scatter and NEC rates were plotted against an effective activity concentration which was calculated by dividing the total activity in the line source by the total volume of the cylindrical phantom in each case. In figure 6(D), the NEC curves for the three cylinders as a function of activity concentration are plotted. Reduced true coincidences were observed because of increased attenuation in the larger cylinders which led to reduced NECR values. The peak NEC rate for the 20, 27 and 35 cm diameter cylinders was 88.5 kcps at 13.7 kBq mL^{-1} (0.370 μCi mL^{-1}), 41 kcps at 9 kBq mL^{-1} (0.24 μCi mL^{-1}) and 16 kcps at 5.8 kBq mL^{-1} (0.16 μCi mL −1), respectively.

Image quality—Results from standard NEMA analysis of the IQ phantom for 4:1 and 8:1 sphere-to-background ratio are shown in figure 7, in addition to representative MR and PET images through the central slice of the IEC phantom. As expected, the tabletop and plastic housing of the phantom is not visible in the MR image (panel A) and the phantom fluid properties are not optimal for MR imaging as evident from the non-uniformity pattern. The attenuation map generated from the MR image is shown in panel B, where the pre-defined tabletop attenuation template is automatically inserted during the image processing chain. The final PET image for the 4:1 phantom is shown in panel C, generated with TOF information and accounting for attenuation, scatter and random events in the system matrix. Qualitatively, the images are comparable to the images obtained on the GEMINI TF PET–CT scanner. Quantitative measurements performed on the data are plotted in panels D and E. CRC and BV (in parentheses) for hot spheres were 31% (8%), 48% (7%), 62% (6%) and 69% (5%) for 4:1 and 47% (6%), 62% (5%), 75% (5%) and 79% (5%) for the 8:1 ratio phantom for the 10, 13, 17 and 22 mm spheres, respectively. Cold sphere contrast recovery and BV (in parentheses) was approximately 75% (5%) and 78% (4%) for the two spheres at both 4:1 and 8:1 hot-to-background ratios. Average lung residual error was approximately 13% for both ratios and is plotted in panel E. There is no significant difference between the results obtained on the image quality phantom when using the Ingenuity TF PET–MR and the GEMINI TF PET–CT scanners.

3.2. Clinical PET–MR imaging

Figure 8 shows whole-body patient images obtained on the PET–MR system using routine clinical imaging protocols. This patient was injected with 367 MBq (9.9 mCi) of ^{18}F-FDG 177 min before PET–MR imaging, and PET data were acquired for 150 s per bed position for a total of 11 bed positions. The patient had malignant lesions in the neck region, which were observed on both the PET–MR and PET–CT images. There were no observed artifacts from the insertion of table and coil templates in the attenuation map. Overall, no noteworthy difference in image quality and identification of abnormal lesions were found between the two PET scans of each case. Details on initial clinical imaging experience with the Ingenuity TF PET–MR are beyond the scope of this paper and are discussed elsewhere (Ratib *et al* 2010).

4. Discussion

The Philips Ingenuity TF PET–MRI system incorporates the Philips time-of-flight GEMINI PET system and Achieva 3T MRI system, and is the world's first clinical whole-body PET–MRI system. The system has been designed to fully utilize the standalone MRI and PET capabilities with no compromise in patient imaging workflow, while maintaining excellent system performance and image quality.

The GEMINI TF PET has previously shown tremendous clinical benefits given its time-of-flight capability (Karp *et al* 2008). The timing resolution of the scanner after recent calibration upgrades is maintained at 525 ps. Daily quality control measurements spread out over several months show that the timing and energy resolution are stable without any considerable variations. Basic performance measurements according to NEMA NU2-2007 procedure showed that the system specifications parallel that of the Philips PET–CT system. SF measurements for the standard 20 × 70 cm cylindrical phantom showed a value of 26%. As this cylinder represents a light patient, we repeated these measurements on larger phantoms with diameters of 27 cm and 35 cm which are representative of average and heavy patients. Increased scatter in these situations was indicated with measured SF values of 35% and 42%, respectively. NECR plots (figure 5) showed that the peak NECR with the NEMA phantom was 88.5 kcps but increased attenuation as well as random and scatter coincidences leads to a noticeable drop in the peak NECR values for the two larger phantoms. Currently, clinical images are acquired at a singles rate of 10–20 Mcps, which is below the singles range (25–30 Mcps) at which the NECR peaks for all three phantoms. We have developed a unique solution for the estimation of attenuation of tabletop and accessories which is essential for both phantom and clinical imaging. The results from the NEMA IQ phantom show the excellent overall imaging performance of the system. Initial results from clinical imaging on the scanner have also yielded acceptable results (Ratib *et al* 2010). The core system performance is comparable to standalone PET and MRI systems, and MR-based attenuation correction represents the major challenge for effective clinical imaging (Zaidi 2007).

PET–MRI systems have been talked about for several years with a few scanner designs and prototypes that have shown promise for preclinical and brain imaging (Shao *et al* 1997, Judenhofer *et al* 2007, Slates *et al* 1999, Catana *et al* 2008, Pichler *et al* 2010, Zaidi *et al* 2010, Schlemmer *et al* 2008). This sequential design obviates some of the more challenging technical issues that have dogged simultaneous systems over the years and have hampered the design of whole-body PET–MRI imaging systems. We successfully mitigated the interference between the two systems to achieve a level of performance equivalent to the standalone PET and MRI systems. Magnetic shielding was introduced in the PET gantry to reduce the magnetic field at the PMTs to a low level such that its residual effect could be calibrated. The shielding was designed such that no material was placed in the normal path of annihilation radiation from within the FOV, preserving system sensitivity. Further modifications were done to relocate electronic circuitry from within the PET gantry to the technical room to reduce the amount of RF noise generated from within the PET–MR room. Such noise gets picked up by the RF coils of the MRI system and manifests itself as spike patterns, noise line patterns, or elevated background noise in the MR images (Wehrl *et al*

2009). Every such noise source was either relocated or shielded for RF emissions. With the magnetically shielded PET system in place, shimming of the B_0 magnetic field followed conventional procedures. The MRI magnet was easily shimmed into specification; this was enabled by judicious placement of the PET gantry at a reasonable distance from the magnet and the smart design of PET magnetic shielding to minimize the steel shield mass. Similarly, no effect on the homogeneity of the MR B_1 or gradient fields was observed. Also, temporal measurements of critical PET and MRI system parameters demonstrated excellent stability of the system.

5. Conclusion

The Ingenuity TF PET–MRI system generates automatically fused PET and MR images, with a sequential imaging workflow parallel to existing hybrid PET systems. There are numerous potential applications for hybrid whole-body PET–MR imaging that have been discussed in detail elsewhere (Schlemmer *et al* 2009). In summary, we describe the design principles and report the PET performance of the Ingenuity TF PET–MRI—the world's first whole-body PET–MR system, as described in the NEMA NU2-2007 guidelines.

Acknowledgments

This work was supported by the Swiss National Science Foundation under grants SNSF 31003A-135576, SNSF 33CM30-124114 and Geneva Cancer League.

References

Catana C, Procissi D, Wu Y, Judenhofer MS, Qi J, Pichler BJ, Jacobs RE, Cherry SR. Simultaneous *in vivo* positron emission tomography and magnetic resonance imaging. Proc. Natl Acad. Sci. USA. 2008; 105:3705–3710. [PubMed: 18319342]

Delso G, Ziegler S. PET/MRI system design. Eur. J. Nuc. Med. Mol. Imaging. 2009; 36:86–92.

DeMeester G, Morich M, McMahon K, Gagnon D. Magnetic shielding for a pet detector system. US Patent Application. 2009:20090195249.

Gagnon D, Morich M, Blakely D, Nieman K. Hybrid PET/MR imaging systems. US Patent Application. 2008:20080312526.

Hofmann M, Pichler B, Scholkopf B, Beyer T. Towards quantitative PET/MRI: a review of MR-based attenuation correction techniques. Eur. J. Nucl. Med. Mol. Imaging. 2009; 36:S93–S104. [PubMed: 19104810]

Hu, Z., et al. MR-based attenuation correction for a whole-body sequential PET/MR system; IEEE Nuclear Science Symp. Conf. Record (NSS/MIC); 2009. p. 3508-3512.

Judenhofer MS, Catana C, Swann BK, Siegel SB, Jung WI, Nutt RE, Cherry SR, Claussen CD, Pichler BJ. Simultaneous PET/MR images, acquired with a compact MRI compatible PET detector in a 7 Tesla magnet. Radiology. 2007; 244:807–814. [PubMed: 17709830]

Judenhofer MS, et al. Simultaneous PET-MRI: a new approach for functional and morphological imaging. Nat. Med. 2008; 14:459–465. [PubMed: 18376410]

Karp JS, Surti S, Daube-Witherspoon ME, Freifelder R, Cardi CA, Adam LE, Bilger K, Muehllehner G. Performance of a brain PET camera based on anger-logic gadolinium oxyorthosilicate detectors. J. Nucl. Med. 2003; 44:1340–1349. [PubMed: 12902426]

Karp JS, Surti S, Daube-Witherspoon ME, Muehllehner G. Benefit of time-of-flight in PET: experimental and clinical results. J. Nucl. Med. 2008; 49:462–470. [PubMed: 18287269]

Matej S, Lewitt R. 3D-FRP: direct Fourier reconstruction with Fourier reprojection for fully 3D PET. IEEE Trans. Nucl. Sci. 2001; 48:1378–1385.

Morich M, DeMeester G, Gagnon D. Hybrid MR/PET with correction for correction for radiation absorption by MR coil. US Patent Application. 2010:20100135559.

NEMA. NEMA Standards Publication NU2-2007: Performance Measurements of Positron Emission Tomographs. Rosslyn, VA: NEMA; 2007.

Pichler BJ, Kolb A, Nagele T, Schlemmer HP. PET/MRI: paving the way for the next generation of clinical multimodality imaging applications. J. Nucl. Med. 2010; 51:333–336. [PubMed: 20150252]

Ratib O, et al. Clinical application of whole body hybrid PET-MR scanner in oncology [abstract]. Eur. J. Nucl. Med. Mol. Imaging. 2010; 37:S220.

Schlemmer HP, Pichler BJ, Krieg R, Heiss WD. An integrated MR/PET system: prospective applications. Abdom. Imaging. 2009; 34:668–674. [PubMed: 18773235]

Schlemmer HP, et al. Simultaneous MR/PET imaging of the human brain: feasibility study. Radiology. 2008; 248:1028–1035. [PubMed: 18710991]

Shao Y, Cherry SR, Farahani K, Meadors K. Simultaneous PET and MR imaging. Phys. Med. Biol. 1997; 42:1965–1970. [PubMed: 9364592]

Slates R, Farahani K, Shao Y, Marsden PK, Taylor J, Summers PE, Williams S, Beech J, Cherry SR. A study of artefacts in simultaneous PET and MR imaging using a prototype MR compatible PET scanner. Phys. Med. Biol. 1999; 44:2015–2027. [PubMed: 10473211]

Surti, S.; Badawi, RD.; Holdsworth, CH.; Fakhri, GE.; Kinahan, PE.; Karp, JS. A multiscanner evaluation of PET image quality using phantom studies; IEEE Nuclear Science Symp. Conf. Record; 2003. p. 2425-2427.

Surti S, Karp J, Freifelder R, Liu F. Optimizing the performance of a PET detector using discrete GSO crystals on a continuous lightguide. IEEE Trans. Nucl. Sci. 2000; 47:1030–1036.

Surti S, Kuhn A, Werner ME, Perkins AE, Kolthammer J, Karp JS. Performance of Philips Gemini TF PET/CT scanner with special consideration for its time-of-flight imaging capabilities. J. Nucl. Med. 2007; 48:471–480. [PubMed: 17332626]

Wehrl H, Judenhofer M, Wiehr S, Pichler B. Pre-clinical PET/MR: technological advances and new perspectives in biomedical research. Eur. J. Nucl. Med. Mol. Imaging. 2009; 36:56–68.

Zaidi H. Is MRI-guided attenuation correction a viable option for dual-modality PET/MR imaging? Radiology. 2007; 244:639–642. [PubMed: 17709821]

Zaidi H, Mawlawi O. Simultaneous PET/MR will replace PET/CT as the molecular multimodality imaging platform of choice. Med. Phys. 2007; 34:1525–1528. [PubMed: 17555233]

Zaidi H, Montandon ML, Alavi A. The clinical role of fusion imaging using PET, CT, MR imaging. Magn. Reson. Imaging Clin. N. Am. 2010; 18:133–149. [PubMed: 19962098]

Zhang, B.; Pal, D.; Hu, Z.; Ojha, N.; Muswick, G.; Tung, CH.; Kaste, J. Attenuation correction for MR table and coils for a sequential PET/MR system; IEEE Nuclear Science Symp. & Medical Imaging Conf; 2009. p. 3303-3306.

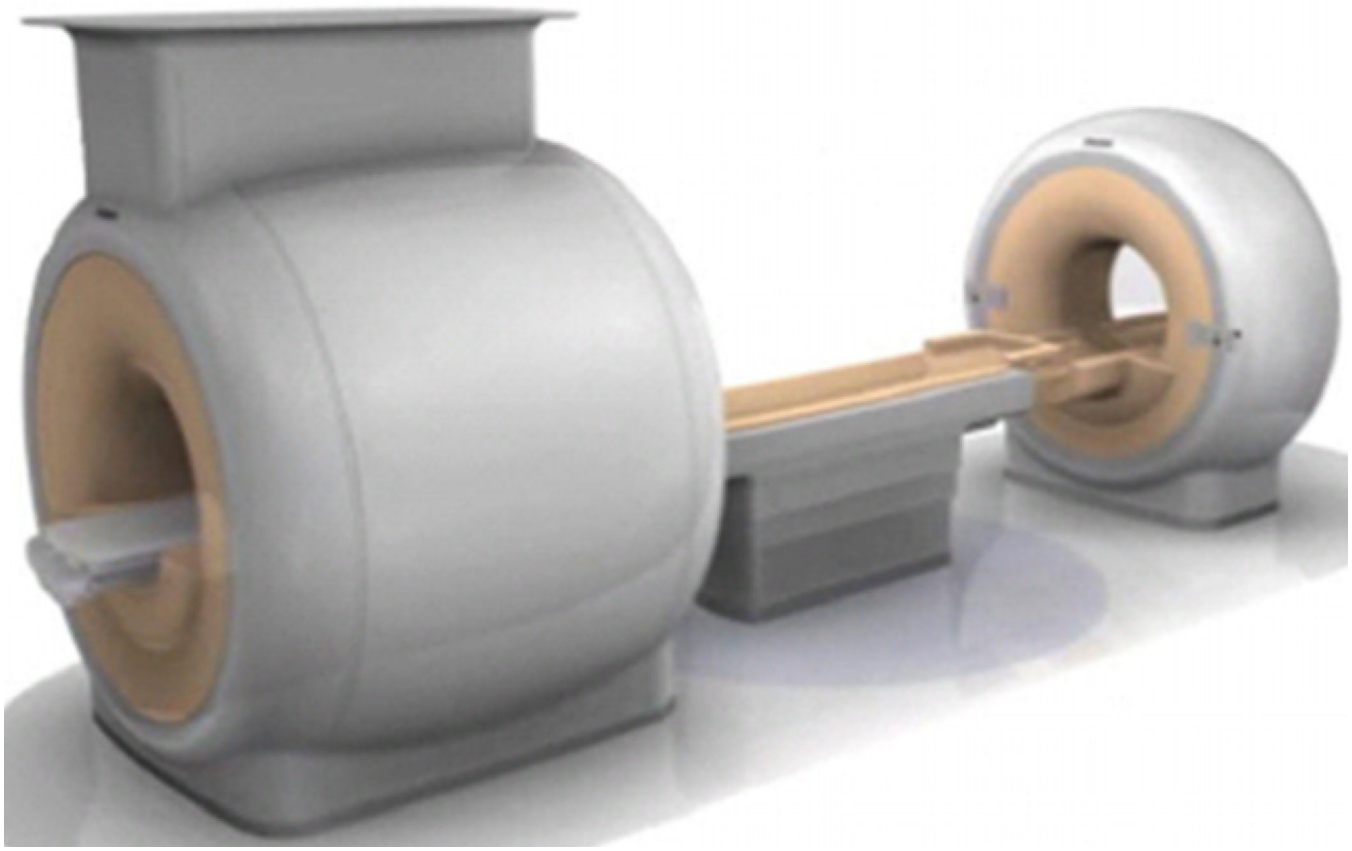

Figure 1.
Illustration of the PET–MRI system. A turntable patient handling system facilitates patient motion between the MRI system on the left and the PET system on the right.

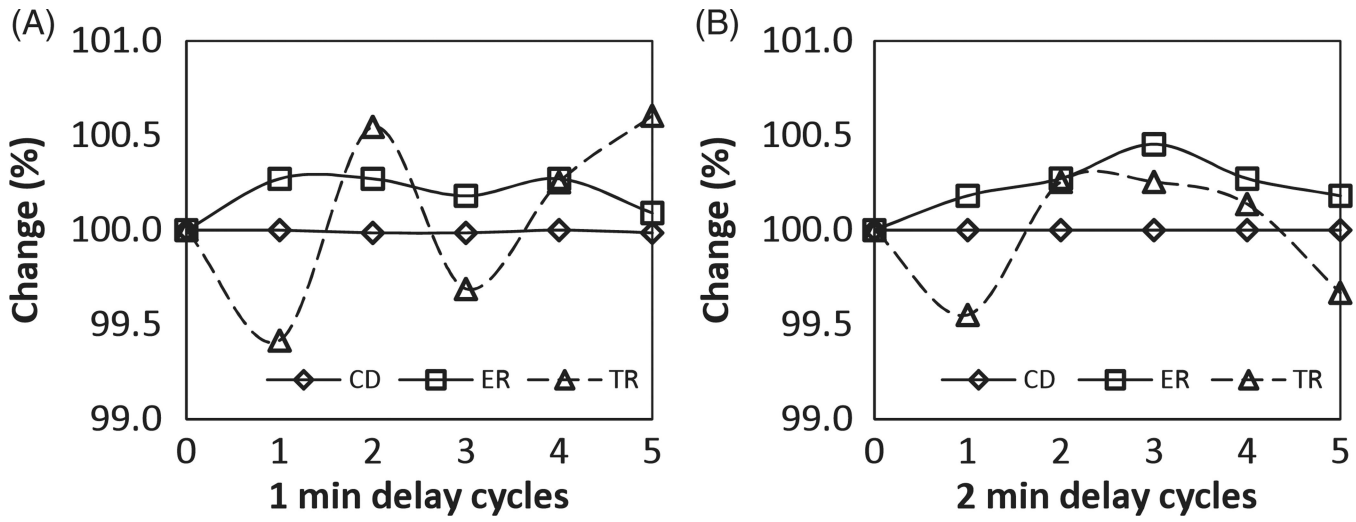

Figure 2.

Count density (CD), energy resolution (ER) and timing resolution (TR) were measured on the PET–MRI system after successful completion of the routine daily quality check procedure. To simulate a typical PET–MRI scanning cycle, the PMT voltage was looped through a sequence of 1 h at low voltage (simulating an MRI exam) and 30 min at standard voltage (simulating a PET exam). Measurements were taken after a delay of 1 min (A) and 2 min (B) of switching back to standard voltage in each cycle, which closely represents the delay time between moving a patient between the MRI and PET scanner. ER and TR after all cycles were well within system specifications, namely 117% and 104%p, respectively.

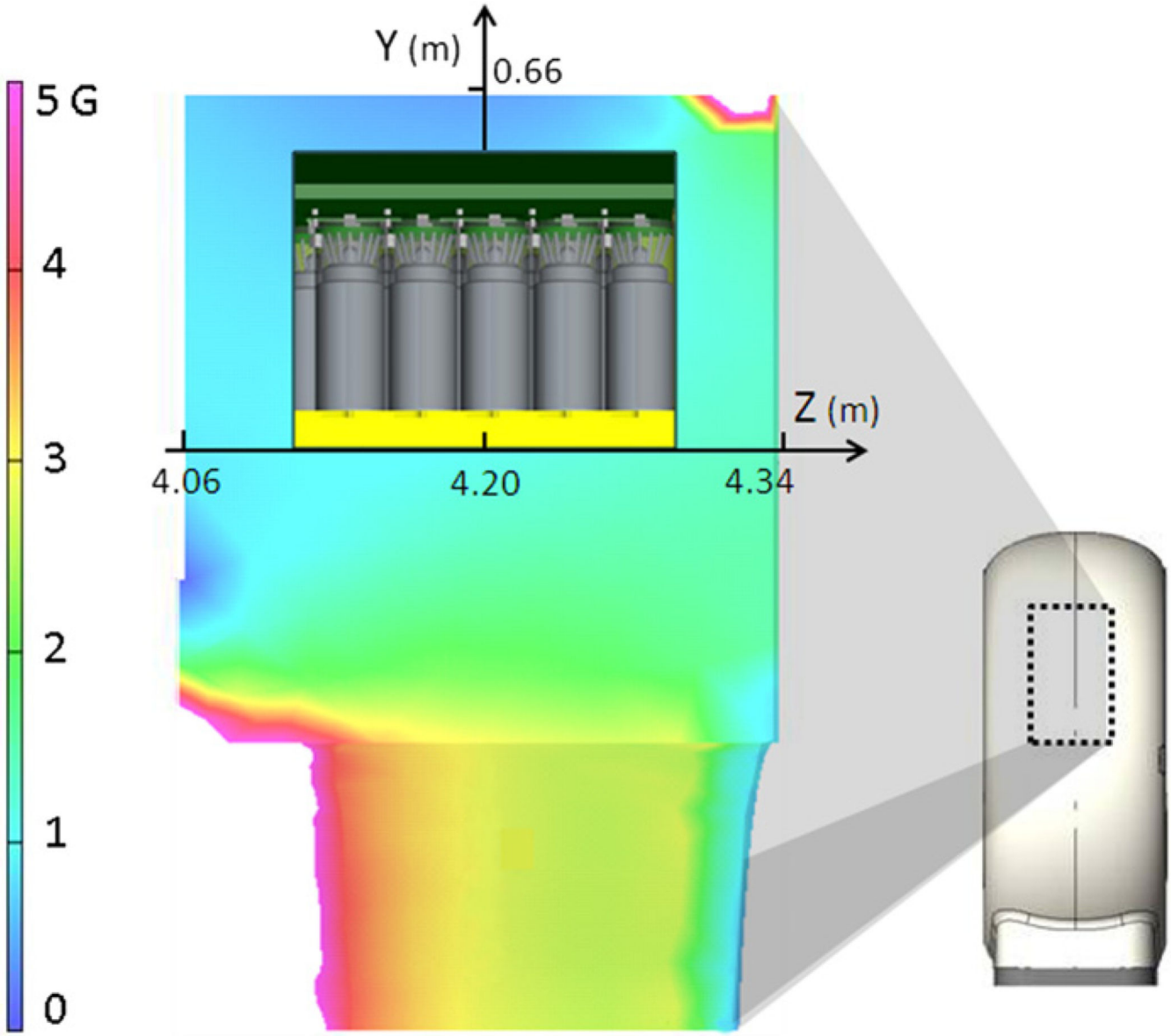

Figure 3.

Magnetic flux density inside the PET gantry. Simulation of the fringe magnetic field of the MRI magnet was done to estimate the magnetic flux density in air around the PMTs. The side-view of the PET gantry is shown on the right with the marked area magnified on the left to show the magnetic flux density around one crystal block and PMTs. With the shielding in place, flux around the PMTs was reduced to acceptable levels between 0.76 G and 1.45 G (before introduction of local PMT shielding).

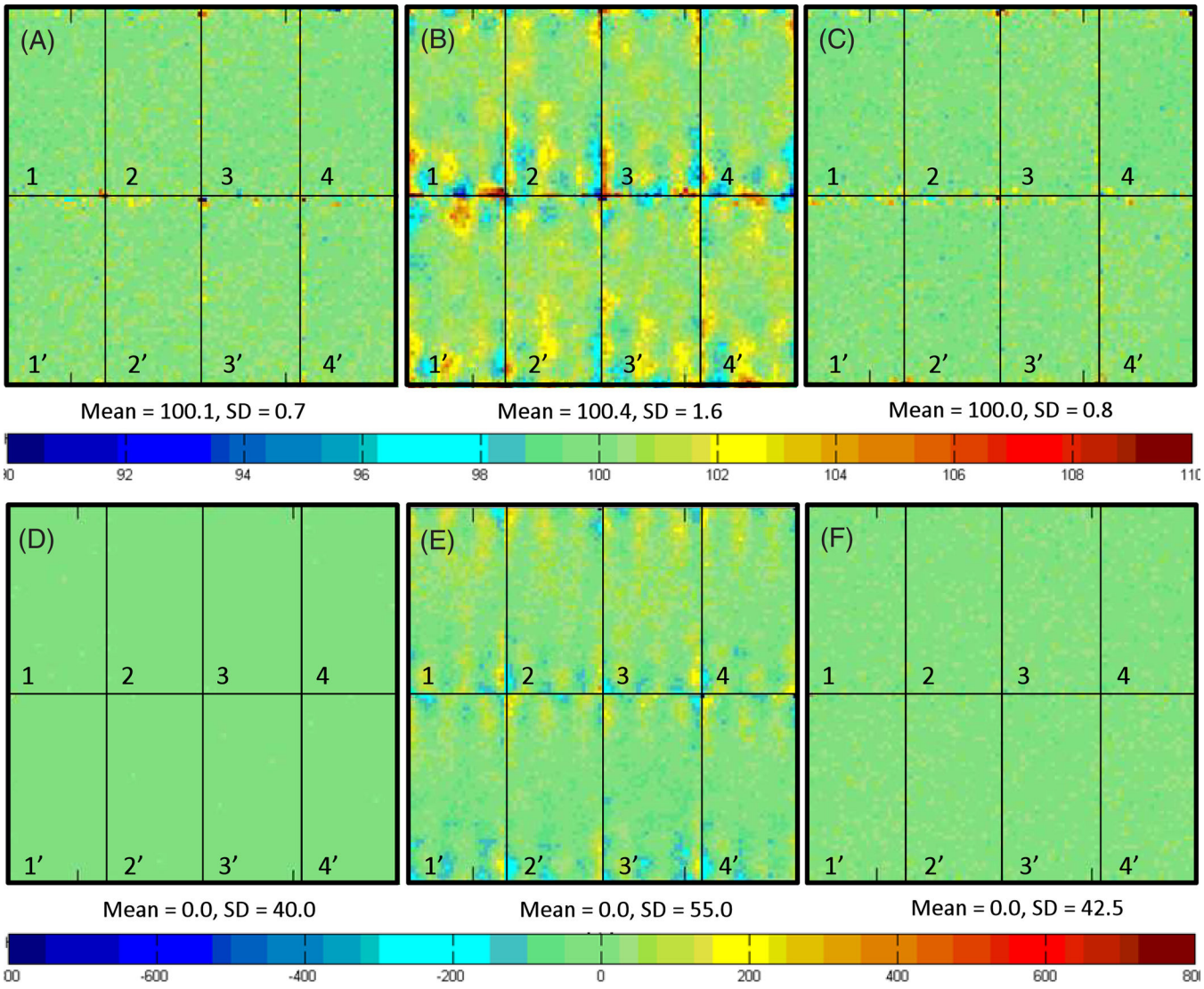

Figure 4.

Energy and timing histogram crystal maps. Measurements with a point source were done to calculate per-crystal energy (top row) and timing histograms (bottom row) of the PET with the MRI magnet ramped down (column 1), MRI magnet ramped up but with original PET calibrations (column 2), and finally after fresh PET calibrations (column 3). In each panel, 4 representative crystal blocks (out of 28) are shown in the top row (numbered 1–4), with diametrically opposite blocks in the bottom row (1′–4′). After PET PMT gains recalibration, the effect of magnetic flux at the PMTs was removed and the crystal energy centroids were brought within a tight range (panel C). Data in figures A–C show energy centroids, which are represented as a percentage of 511 keV. Similar results were obtained from plotting the per-crystal timing resolution histograms of the PET scanner where recalibration of the PET after MRI magnet ramp-up resulted in recovery of timing resolution centroids of the system (panel F). Results presented in panels D–F represent the timing resolution (in ps) between a pair of coincidence photons which are recorded in the PET system.

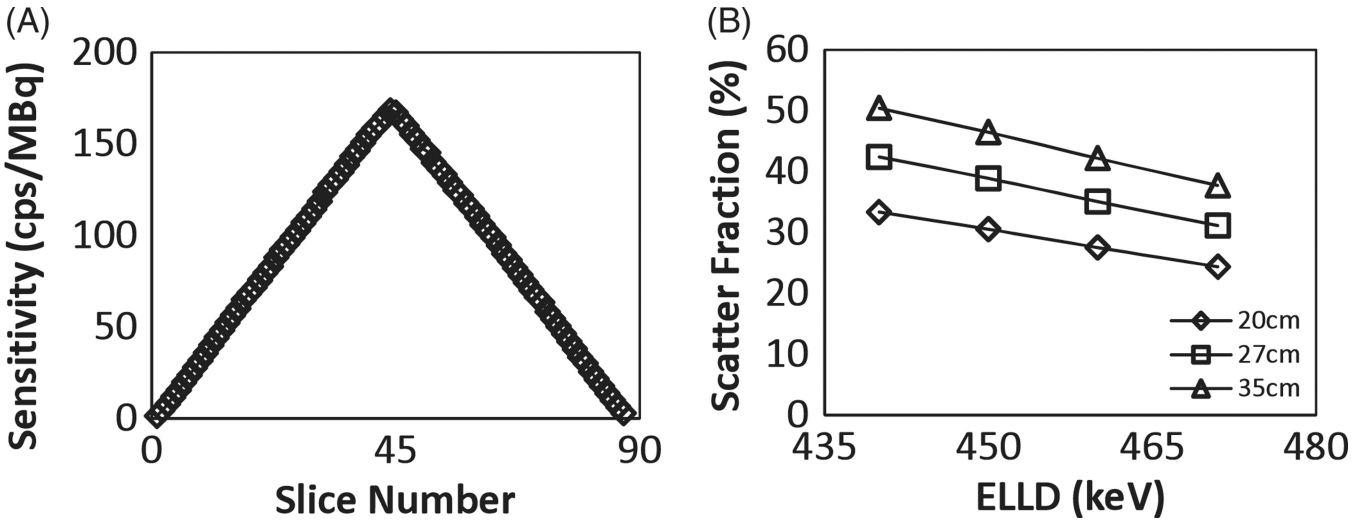

Figure 5.

(A) Triangular sensitivity profile as measured with the NEMA NU2-2007 line source. (B) Plot of the measured SF as a function of ELLD for three different cylinder diameters as shown in the legend.

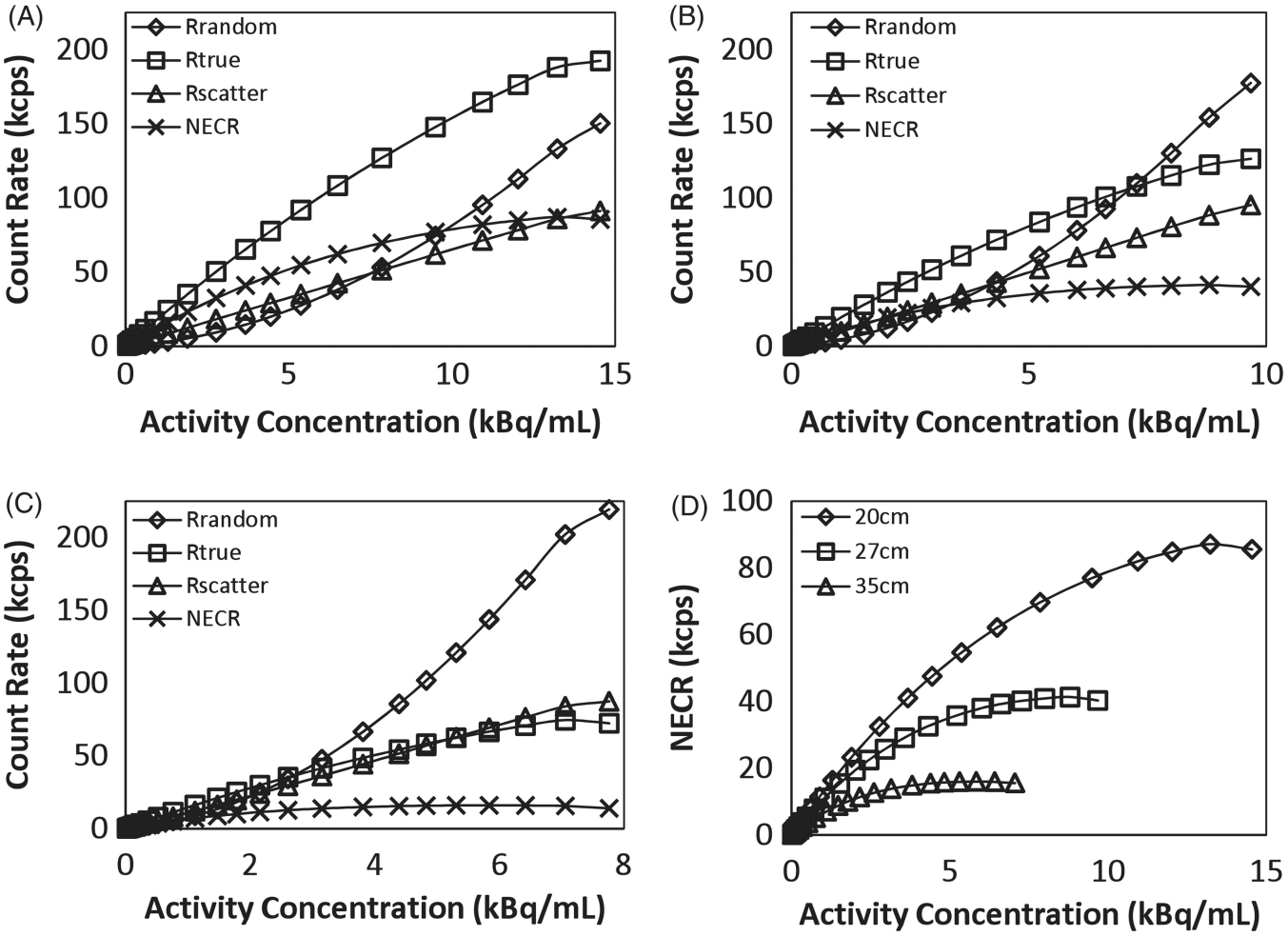

Figure 6.

Plot of counting rates as a function of activity concentration for 20 cm (A), 27 cm (B) and 35 cm (C) diameter cylinders. True coincidence rates, random coincidence rates, scatter coincidence rates and NEC rates are plotted. (D) Summary plots for NEC rates as a function of activity concentration in the scanner for the three different cylinders.

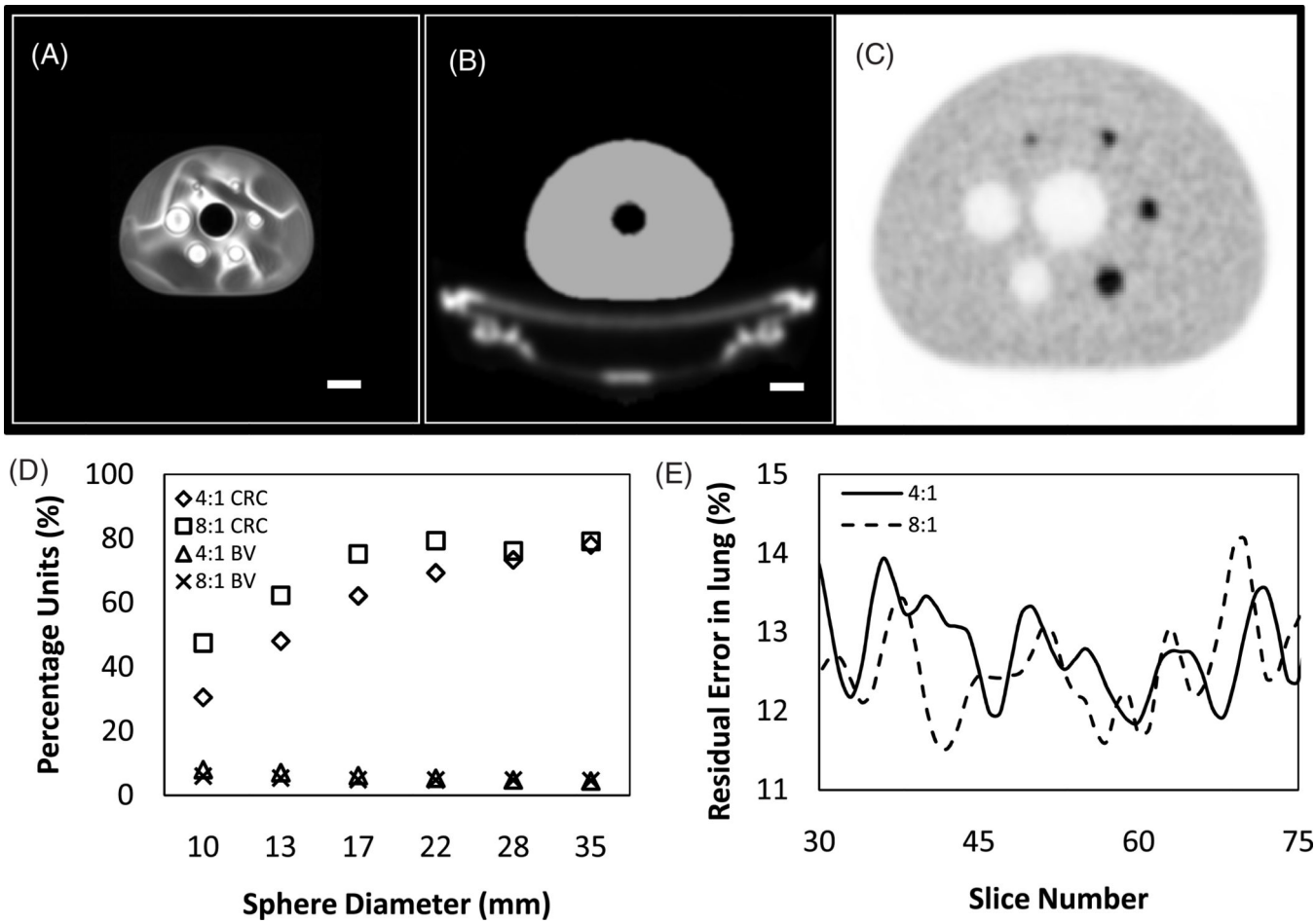

Figure 7.

(A) Central slice from *atMR* images of the NEMA IEC body phantom. Imaging parameters were as described in the text. Note that the plastic housing of the phantom and tabletop are not visible in the *atMR* images. Scale bar = 40 mm. (B) Attenuation map generated from the *atMR* image. A pre-generated attenuation template of the tabletop was inserted into the image, in addition to the extension of the body of the phantom to account for plastic housing. Scale bar = 40 mm. (C) PET image of the phantom (with 4:1 hot-to-background ratio) using default Philips NEMA acquisition and reconstruction protocol for Ingenuity TF PET systems. The image is magnified by a factor of 2 compared to panels A and B. (D) CRC and BV numbers for the 4:1 and 8:1 hot-to-background ratio IEC phantoms. (E) Residual error in lung insert for the central slices of the phantom calculated for 4:1 and 8:1 ratio phantoms.

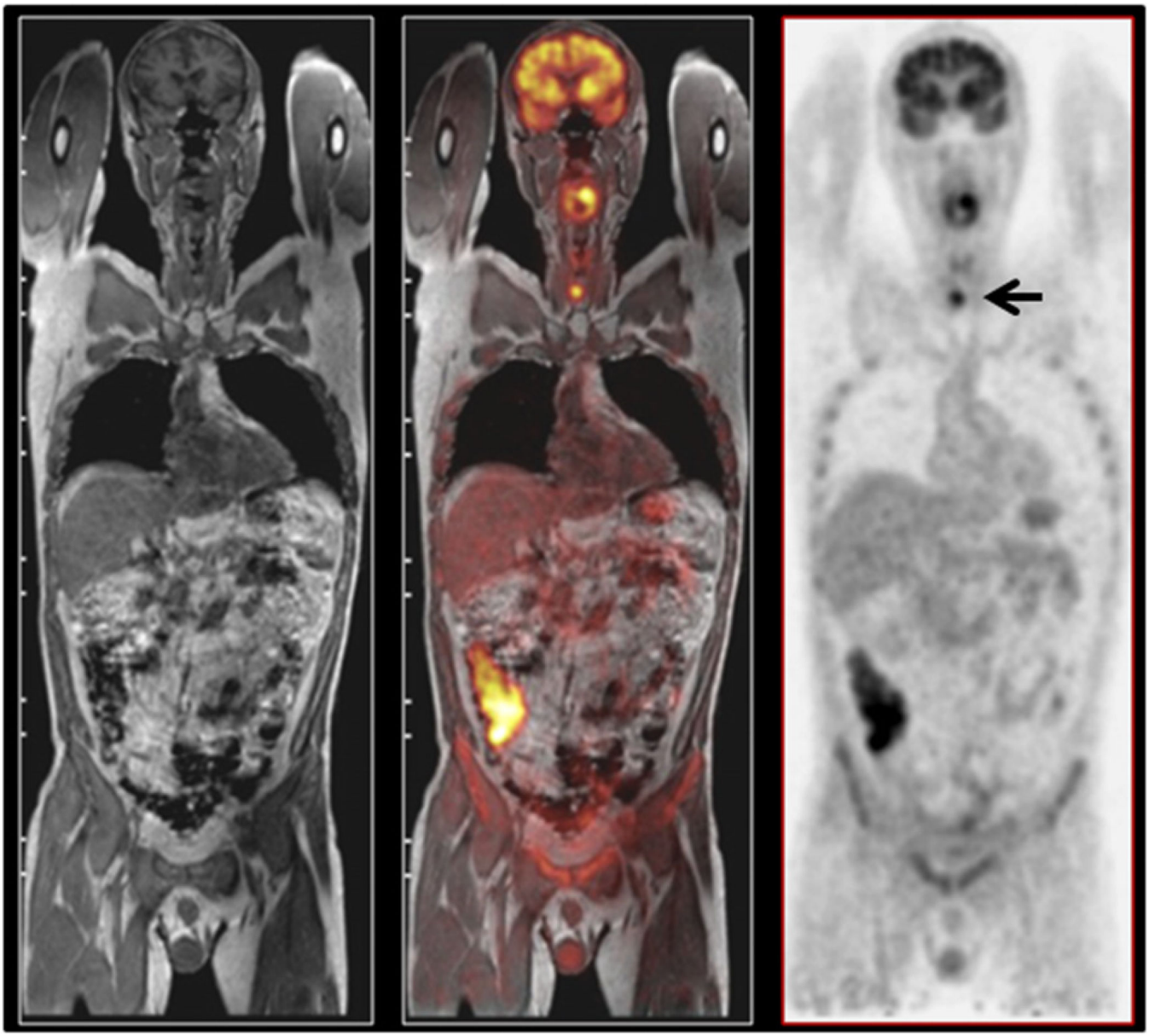

Figure 8.

Coronal whole-body images for a patient with malignant lesions in the neck region. MRI (left), PET (right) and fused PET–MRI images (center) are shown. The patient was injected with 367 MBq (9.9 mCi) of ^{18}F-FDG 177 min before PET–MRI scan time. PET images were acquired for 150 s per bed position for a total of 11 bed positions.

Table 1

MRI characteristics of the Philips Achieva 3T-X MRI system.

MRI parameter	Description
Magnet type	Superconducting 3T
Bore diameter (cm)	60
Maximum FOV (cm)	50 × 50 × 45
Field homogeneity (V_{RMS} [a])	0.5 ppm
40 × 40 × 40 Volume (cm)	
Max gradient amplitude (mT m^{-1}) and slew rate (mT m^{-1} ms^{-1}) on each axis	Standard mode = 40/100 Enhanced mode = 80/200
Number of receive channels	16 standard, 32 optional
Channel bandwidth	3 MHz per channel
Table weight capacity	200 kg

[a]Measured in 24 angles on 24 planes.

Table 2

PET characteristics of the Philips Ingenuity TF system.

PET parameter	Description
Detector ring diameter	90.3 cm
Bore diameter	70.7 cm
Axial FOV	18 cm
Crystal type	LYSO
Crystal size and type	$4 \times 4 \times 22$ mm^3
Crystal array per module	23 × 44
No of detector modules	28
No of individual crystals	28 336
Coincidence window width	6 ns
Energy acquisition window	460–665 keV

Table 3

Measurement of the MRI magnet main magnetic field B0 homogeneity in the FOV after the standard MRI shimming procedure before and after the PET gantry was installed in the PET–MR suite. B0 homogeneity was calculated on the characterization volumes based on spherical harmonic representation of the data, as determined from 24-plane, 24-angle measurements on a larger volume.

Volume dimensions (*X/Y/Z*, each in cm)	**Standalone MRI (V_{rms}, ppm)**	**After PET installation (V_{rms}, ppm)**	**MRI specification (V_{rms}, ppm)**
40 × 40 × 40	0.37	0.32	<0.5
30 × 30 × 30	0.07	0.08	<0.12
20 × 20 × 20	0.014	0.017	<0.03
10 × 10 ×10	0.002	0.002	<0.004

Table 4

Overall system energy and timing resolution (FWHM) with the MRI magnet ramped up and PET recalibration.

	Change after MRI ramp (%)	Measured value
Energy resolution	0.22 ± 5.08	11.6 ± 0.1%
Timing resolution	1.3 ± 0.6	523.3 ± 11.6 ps

Table 5

Results of PET spatial resolution measurements with a point source on the Ingenuity PET–MRI system compared to the GEMINI TF PET–CT system.

	Ingenuity TF PET–MR		GEMINI TF PET–CT (Surti *et al* 2007)	
Spatial resolution	**FWHM (mm)**	**FWTM (mm)**	**FWHM (mm)**	**FWTM (mm)**
Transverse (1 cm)	4.7 ± 0.1	9.4 ± 0.2	4.8	9.7
Axial (1 cm)	4.6 ± 0.1	9.5 ± 0.1	4.8	9.6
Radial (10 cm)	5.0 ± 0.1	9.9 ± 0.1	5.2	10.3
Axial (10 cm)	5.0 ± 0.1	9.7 ± 0.1	4.8	9.6
Tangential (10 cm)	5.3 ± 0.1	10.5 ± 0.1	5.2	10.2